https://doi.org/10.5194/egusphere-2024-1220
Preprint. Discussion started: 23 May 2024

Analysis of surface deformation prediction in high mountain canyon areas based on time-series InSAR technology and improved Elman neural network

Kuayue Chen[1], Wenfei Xi[2], Baoyun Wang[1,3]

[1]School of Mathematics, Yunnan Normal University, Kunming, People's Republic of China
[2]Faculty of Geography, Yunnan Normal University, Kunming, People's Republic of China
[3]Yunnan Key Laboratory of Modern Analytical Mathematics and Applications, Kunming, People's Republic of China

Correspondence to: Baoyun Wang (wspbmly@163.com)

Abstract. To address the issues of over-reliance on deformation data and model singularity in existing surface deformation prediction methods in high mountain canyon areas, this study proposes the improvement of Elman neural network using cuckoo search algorithm and grey wolf optimization algorithm (CS-Elman and GWO-Elman) from the perspective of multi-temporal and multi-factor analysis. Firstly, surface deformation in the study area is monitored using SBAS-InSAR and PS-InSAR techniques. Then, the optimal evaluation factors are determined from 13 evaluation factors including digital elevation model (DEM) and slope using grey correlation analysis and correlation matrix analysis in SPSSAU software. These optimal factors, combined with surface deformation monitoring values obtained from InSAR technology, are used to construct CS-Elman and GWO-Elman prediction models from a multi-factor and multi-temporal perspective. Finally, the optimal prediction model is determined through comparative experiments and its prediction performance is validated. Results indicate: (1) SBAS-InSAR and PS-InSAR techniques exhibit a high correlation coefficient (R^2=0.85) between monitored radar line of sight (LOS) deformation rates, demonstrating the feasibility of joint analysis of the two techniques. (2) The CS-Elman model has a smaller absolute error range compared to the GWO-Elman model. The optimal convergence iteration number, mean square error, mean absolute error (MAE) and mean absolute percentage error (MAPE) of the CS-Elman model are 3 iterations, 0.020 mm/a, 1.620 mm/a and 21.500%, respectively, which are all superior to the GWO-Elman model. This indicates that the Elman network optimized by the CS algorithm exhibits better performance and higher accuracy in predicting surface deformation in high mountain canyon areas. (3) Comparative analysis with SVM, LSTM and PSO-BP models, as well as prediction of temporal deformation trends at deformation points, validate the advantages and effectiveness of the CS-Elman model in surface deformation prediction. This method can serve as an effective means for long-term deformation prediction in high mountain canyon areas.

Keywords. Small baseline subset interferometric synthetic aperture radar (SBAS-InSAR); Persistent scatterer interferometric synthetic aperture radar (PS-InSAR); Elman neural network; Deformation monitoring; Predictive analysis; Geological hazard

https://doi.org/10.5194/egusphere-2024-1220
Preprint. Discussion started: 23 May 2024

1 Introduction

China is a country prone to geological disasters, and various types of geological disasters have caused enormous losses to the lives and property security of its people (Derbyshire, 2001; Xu and Wang, 2022; Liu and Wang, 2024). Landslides, debris flows and collapses are major geological disasters characterized by strong concealment, significant hazards and high suddenness, and they are widely distributed in mountainous areas and canyons in China (Jiang et al., 2022; Guo et al., 2016). Therefore, monitoring and early warning of geological disasters in high mountain canyon areas have become particularly important (An et al., 2022). The significance lies in the ability to identify potential hazard points of landslides, debris flows and other geological disasters in advance, and to take appropriate measures to reduce the probability of disasters and minimize the loss of life and property.

In geological disaster monitoring and debris flow research, surface deformation directly reflects the current stability and movement status of slopes (Wang et al., 2020; Tao et al., 2021). Therefore, by monitoring surface deformation, critical information can be provided for identifying potential risks of geological disasters such as landslides and debris flows. Traditional monitoring methods, such as the global positioning system (GPS) (Kim et al., 2003) and precise leveling measurements (Vanicek et al., 1980), suffer from drawbacks such as low accuracy, high workload and limitations imposed by terrain conditions. Meanwhile, traditional methods are unable to effectively monitor large-scale surface deformation (Yang et al., 2020; He et al., 2022b). Compared to traditional methods of surface deformation monitoring, interferometric synthetic aperture radar (InSAR) technology possesses all-weather and all-day characteristics. It enables the direct spatial acquisition of extensive and high-precision terrain elevation and deformation information (Osmanoğlu et al., 2016; Zhang et al., 2022; Zhang et al., 2022). Currently, numerous scholars have made significant progress in monitoring natural disasters such as earthquakes, landslides and debris flows using InSAR technology (Nikolaeva et al., 2014; Huang et al., 2019; Suresh and Yarrakula, 2020; Yang et al., 2023). On the contrary, in terms of surface deformation prediction, the majority of studies are based on constructing prediction models using time-series deformation data, with only a few adopting a model-building approach from the perspective of deformation influencing factors. Ye et al. (2022) analyzed the spatiotemporal characteristics of ground deformation along the Zhengzhou subway line using PS-InSAR technology. They then utilized inverse distance interpolation and equalization processing and applied a long short-term memory (LSTM) model to predict and analyze typical deformation points. Their findings validated that compared to grey models, the LSTM model exhibits higher fitting and prediction accuracy. Yang et al. (2022) utilized InSAR technology to monitor the deformation information of the Meili Snow Mountain Glacier from 2020 to 2021. They established a prediction model based on genetic algorithm-back propagation (GA-BP) neural networks and found that the optimized prediction model significantly improved accuracy. Teng et al. (2022) utilized SBAS-InSAR surface deformation monitoring data from the Hefei City to construct training samples. They established an Elman model and experimental results showed that the predicted deformation values of

https://doi.org/10.5194/egusphere-2024-1220
Preprint. Discussion started: 23 May 2024

the Elman model were in basic agreement with the monitoring values. Radman et al. (2021) utilized SBAS-InSAR technology to obtain surface deformation information around Lake Urmia. They combined environmental factors such as rainfall, groundwater and lake area, and used three models, namely multilayer perceptron (MLP), convolutional neural network (CNN) and LSTM, to predict land deformation. The effectiveness and robustness of the ensemble model were validated through mean absolute error and root mean square error. Wang et al. (2019) utilized SBAS-InSAR technology to acquire surface deformation characteristics in the Erhai Lake region from 2015 to 2018. They selected building area, water level, rainfall and temperature as inputs to the back propagation (BP) neural network for predicting surface deformation. While the aforementioned methods can effectively predict surface deformation information, they all have certain drawbacks and limitations. Some scholars (Teng et al., 2022; Yang et al., 2022; Ye et al., 2022) have proposed prediction models that overly rely on deformation data, considering fewer other factors that may trigger disasters. They solely utilize deformation data as input and output layers for prediction, which has certain limitations. Conversely, other scholars (Wang et al., 2019; Radman et al., 2021), while constructing prediction models from the perspective of influencing factors, are unable to predict multi-period deformation trends at specific points in the study area. Therefore, when predicting surface deformation, it is necessary to consider multiple factors that influence deformation.

In high mountain canyon areas, surface deformation exhibits nonlinear characteristics, leading to the complexity of natural disasters such as landslides and debris flows. Merely utilizing time-series deformation data as input for prediction models often yields unsatisfactory results in studying surface deformation in disaster-prone areas. Therefore, it is essential to consider major causative factors influencing deformation, such as slope, soil type and vegetation coverage. Additionally, surface deformation prediction typically involves a set of data correlated with time series. Hence, selecting appropriate prediction models can effectively enhance prediction accuracy. The Elman neural network is a typical type of local regression network. It adds a feedback layer acting as a delay operator to the basis of the BP neural network, enabling it to memorize information and thereby adapt to time-varying characteristics. This improvement enhances the network's global stability, providing significant advantages when handling time-series foundational data such as surface deformation (Ding et al., 2013; Jia et al., 2019). However, determining the weights, thresholds and learning rates of the Elman neural network is often challenging, requiring optimization. The cuckoo search (CS) algorithm (Mareli and Twala, 2018) and grey wolf optimizer (GWO) algorithm (Gupta and Deep, 2019) are chosen to search for the optimal weights, thresholds and learning rates of the Elman neural network, aiming to enhance the model's prediction accuracy for surface deformation variables.

In summary, this study utilizes time-series InSAR technology and an improved Elman neural network algorithm to monitor and predict surface deformation in high mountain canyon areas. It proposes a predictive model constructed from multiple time-series and factors. Specifically, the study processes the research area using InSAR technology to obtain subsidence areas and annual deformation rate maps. These are combined with relevant influencing factors as input layers, while the

https://doi.org/10.5194/egusphere-2024-1220
Preprint. Discussion started: 23 May 2024

annual deformation rate serves as the output layer, establishing the relationship between influencing factors and deformation rate prediction models.

2 Research Methodology

The main technical process of this study includes: (1) Acquisition of surface deformation information in the study area. (2) Selection of evaluation factors. (3) Construction of CS-Elman and GWO-Elman models. The overall technical process is illustrated in Figure 1.

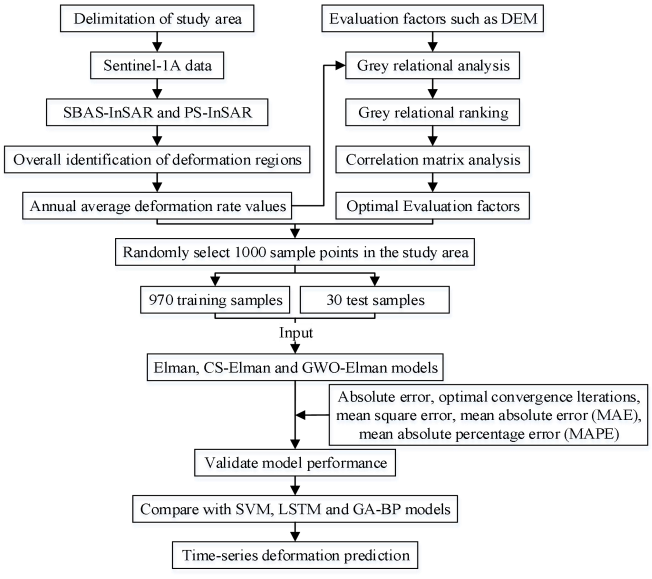

Figure 1: Overall technical flowchart.

2.1 Acquisition of surface deformation information in the study area

This study firstly employs SBAS-InSAR technology to extract surface deformation information in the study area, and then utilizes PS-InSAR technology to extract deformation variables for validation. By comparing and correlating the deformation results obtained from the two techniques, detailed information regarding surface deformation in the study area is obtained.

The SBAS-InSAR technology is a method proposed by Berardino et al. (2002) in 2002 for surface deformation monitoring. Firstly, coherent target points with stable scattering characteristics are extracted from a long time series of multiple SAR images. Secondly, a multi-master image strategy is employed to combine as many small datasets as possible based on small spatio-temporal baseline thresholds. Thirdly, in the deformation solving process, the singular value decomposition method (Akritas and Malaschonok, 2004) is used to process the time series data of the study area. Finally, surface deformation

https://doi.org/10.5194/egusphere-2024-1220
Preprint. Discussion started: 23 May 2024

information of the study area is extracted from the time series data processed by singular value decomposition (Lanari et al., 2004).

The PS-InSAR technology, proposed by Ferretti et al. (2001) in 2001, is a technique designed for analyzing persistent scatterers (PS). Its basic principle involves selecting the SAR image with the best spatio-temporal coherence as the reference image among N scenes, while the others are auxiliary images, forming N-1 differential interferograms. Then, points with high phase quality over the time series are selected and a function model is established. The model is analyzed and solved to obtain surface deformation values.

The SBAS-InSAR technology provides large-scale continuous spatial deformation results, while the PS-InSAR technology provides deformation information for individual pixel points. Utilizing surface deformation information obtained from different time-series InSAR technologies can complement each other, resulting in more accurate and comprehensive monitoring results.

2.2 Selection of evaluation factors

Surface deformation is influenced by multiple factors, which exhibit diversity and complexity. Moreover, certain factors may exhibit correlations, and high correlations can lead to model complexity and reduced operational speed. Therefore, conducting correlation analysis among various factors is crucial. By analyzing the correlations among factors, it is possible to exclude highly correlated factors, which is significant for model establishment and surface deformation monitoring (Ulusay et al., 1994).

Based on the geological environmental background of the study area, this study selected factors closely related to the formation of debris flows, including digital elevation model (DEM) data, slope, aspect, curvature, soil type, topographic wetness index (TWI), stream power index (SPI), surface roughness, terrain relief, fractional vegetation cover (FVC), rainfall, lithology and vegetation type, as factors for surface deformation in the study area. First, the ArcGIS software was used to extract the raster data of each factor in the study area. Next, the SPSSAU software was employed to conduct grey relational analysis on the 13 factors with the deformation values monitored by InSAR technology separately, obtaining the grey relational degree ranking, and selecting factors with high correlation to the deformation values. Finally, the bivariate correlation analysis tool was used to analyze the correlation matrix of the above factors, eliminating highly correlated factors and obtaining the optimal evaluation factors. The correlation coefficient R was used to measure the degree of correlation between each factor, selecting more suitable factors to construct CS-Elman and GWO-Elman models with the deformation values. The range of R is [-1, 1]. When $R > 0$, the factors are positively correlated, when $R < 0$, the factors are negatively correlated, and when $R = 0$, it indicates no linear correlation. The closer $|R|$ is to 1, the higher the correlation is. The specific range of R and its correlation are shown in Table 1.

https://doi.org/10.5194/egusphere-2024-1220
Preprint. Discussion started: 23 May 2024

Table 1: Range of *R* values and correlation table.

Correlation coefficient	Range of values	Correlation
R	(0,1]	Positive correlation
	0	No linear correlation
	[-1,0)	Negative correlation
|*R*|	(0,0.5]	Low correlation
	(0.5,0.8]	Significant correlation
	(0.8,1]	High correlation

2.3 Construction of improved Elman network model

2.3.1 Elman neural network

The Elman neural network, a type of recurrent neural network (RNN), incorporates a feedback layer into its structure, consisting of an input layer, a hidden layer, a feedback layer and an output layer (Elman, 1990). With the presence of the feedback layer, the Elman network can retain previous information relative to conventional neural networks, making it more suitable for processing sequential data. It can better capture the temporal characteristics and dependencies in the data. The structure of the Elman neural network is illustrated in Figure 2.

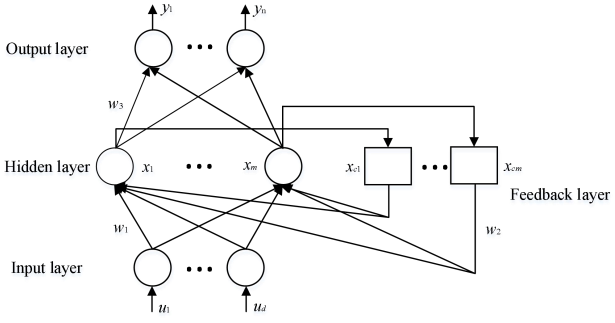

Figure 2: Elman neural network structure.

In this representation, $[u_1,u_2,...,u_d]$ represents the input vector; $[x_1,x_2,...,x_m]$ represents the hidden layer node vector; $[x_{c1},x_{c2},...,x_{cm}]$ represents the feedback layer node vector; and $[y_1,y_2,...,y_n]$ represents the output vector. w_1, w_2 and w_3 denote the connection weights from the input layer to the hidden layer, from the feedback layer to the hidden layer, and from the hidden layer to the output layer, respectively.

The mathematical model of the Elman neural network is as follows in equations (1) to (3):

$$y(k) = g[w_3 x(k) + b_2] \tag{1}$$

https://doi.org/10.5194/egusphere-2024-1220
Preprint. Discussion started: 23 May 2024

$$x(k) = f[w_2 x_c(k) + w_1 u(k-1) + b_1] \tag{2}$$

$$x_c(k) = x(k-1) \tag{3}$$

In the equations, $y(k)$ represents the network output; $x(k)$ represents the hidden layer output; $u(k)$ represents the external input; b_1 and b_2 are the thresholds for each layer; g and f represent the transfer functions of the output neurons and hidden layer neurons, respectively.

2.3.2 Cuckoo search algorithm

The cuckoo search (CS) algorithm, proposed by Yang et al. (2009) in 2009, is a population-based optimization algorithm. It features simplicity in design, requiring fewer parameters, and is insensitive to parameter changes, exhibiting good stability. It is less likely to get stuck in local optima and is applicable to both continuous and discrete optimization. The characteristics of nest-parasite behavior observed in cuckoos inspire the algorithm's approach: cuckoos lay their eggs in other birds' nests, relying on host birds to incubate them; if a host discovers the foreign egg, it will abandon the nest. The algorithm's steps can be summarized as follows: (1) Each cuckoo lays one egg at a time during breeding and randomly selects a nest to lay the egg. (2) In each nest, only the highest-quality eggs are retained to breed the next generation. (3) The number of parasitic nests is fixed, and if a host bird discovers a foreign egg, the nest is abandoned.

The *Levy* flight of cuckoos is a biological description used in the updating process of the cuckoo search algorithm to avoid falling into local optima. The flight formula of cuckoos is represented in equation (4):

$$x_i^{t+1} = x_i^t + \alpha \oplus Levy(\lambda) \tag{4}$$

In the equation, x_i^t represents the position of the ith nest at generation t, where i=1,2,...,n. α denotes the step size, which is a positive number typically set to 1. $\oplus$ denotes pointwise multiplication. $Levy(\lambda)$ is the random search path, generating step sizes that follow a Levy distribution, as shown in equation (5):

$$Levy(\lambda) \sim u = t^{-\lambda}, 1 < \lambda \leq 3 \tag{5}$$

The characteristic of *Levy* flight is that the step size is random. Larger step sizes can ensure a certain probability of escaping from local optima, thus obtaining the global optimum solution.

2.3.3 Grey wolf optimizer algorithm

The grey wolf optimizer (GWO) algorithm is a population-based metaheuristic algorithm proposed by Mirjalili et al. (2014) in 2014, inspired by the social hierarchy of grey wolf populations. In the social hierarchy of grey wolves, there are four different types of wolves, including α, β, δ and ω wolves, with their social status decreasing from left to right. The four ranks of wolf packs represent the four solutions searched during the GWO optimization process, representing the optimal solution, good solution, suboptimal solution and candidate solution, respectively.

https://doi.org/10.5194/egusphere-2024-1220
Preprint. Discussion started: 23 May 2024

The GWO algorithm mainly consists of three steps: encircling, hunting and attacking. The behavior of grey wolves can be defined in mathematical models, as shown in equations (6) and (7):

$$D = \left| C \cdot X_p(t) - X(t) \right| \tag{6}$$

$$X(t+1) = X_p(t) - A \cdot D \tag{7}$$

In the equations, D represents the distance between the grey wolf and the prey; A and C are coefficient vectors, which can be calculated respectively by equations (8) and (9); t denotes the iteration number; $X_p(t)$ and $X(t)$ represent the position vectors of the prey and the grey wolf after t iterations, respectively; $X(t+1)$ denotes the position vector of the grey wolf after $t+1$ iterations.

$$A = 2a \cdot r_1 - a \tag{8}$$

$$C = 2 \cdot r_2 \tag{9}$$

In the equations, r_1 and r_2 are random vectors within the range [0,1]; a is the convergence factor, which linearly decreases from 2 to 0 as the number of iterations increases, calculated as shown in equation (10):

$$a = 2 - \frac{2t}{T_{\max}} \tag{10}$$

In the equation, $T_{\max}$ represents the maximum number of iterations.

2.3.4 CS/GWO-Elman neural network

Elman neural network demonstrates outstanding performance in handling time-series data and tasks related to time. But it also suffers from issues such as vanishing gradients, slow training speeds and susceptibility to local minima. To address these challenges, this paper utilizes CS and GWO algorithms to optimize the initial weights and thresholds of Elman network. These optimized parameters are then applied to the Elman neural network, ultimately producing values that meet the required accuracy. The workflow is illustrated in Figure 3.

The specific steps of the CS-Elman neural network are as follows:

Step 1: Divide the data into training and testing sets, and normalize the data.

Step 2: Construct the Elman neural network, select relevant data as input and output, and initialize the weights and thresholds of the neural network.

Step 3: Given the number of nests n, randomly generate n nests $X_0 = (x_1^0, x_2^0, \cdots x_n^0)^{\mathrm{T}}$ within a given range, where the relevant variables represent the weights and thresholds of the neural network. During the training process, optimize these parameters to find the optimal nest positions x_b^0.

Step 4: Utilize the *Levy* flight method to update the nest positions, generating new nests $X_0 = (x_1^t, x_2^t, \cdots x_n^t)^{\mathrm{T}}$. Calculate the fitness of the new nests and compare them with the previous generation. If the fitness of the new nests is better, update their

https://doi.org/10.5194/egusphere-2024-1220
Preprint. Discussion started: 23 May 2024

positions; otherwise, retain the positions of the previous generation.

Step 5: Generate a new solution F_i and compare it with the candidate solution F_j. If F_j>F_i, do not update the nest positions; if F_i>F_j, update the nest positions. When updating the nest positions, also compare them with the positions of the previous generation. Retain the new nest positions if they are better; otherwise, do not change the nest positions.

Step 6: Return the parameters of nest positions that meet the iteration limit or error condition to the Elman neural network as the optimal weights and thresholds.

The specific steps of the GWO-Elman neural network are as follows:

Steps 1 and 2 are the same as those in the CS-Elman neural network.

Step 3: Set the parameters of the GWO algorithm, including the number of grey wolves in the population, the upper and lower bounds of the grey wolf dimensions, the dimensions of individual grey wolf position information and the maximum number of iterations.

Step 4: Select the fitness function, calculate the fitness, and select the optimal wolf (α), the superior wolf (β) and the inferior wolf (δ).

Step 5: Update the positions of the remaining wolves (ω), and update the parameters A, C and a.

Step 6: Map the position of the optimal wolf (α) that meets the iteration count or error condition to the weight matrix and return it to the Elman neural network as the optimal weights and thresholds.

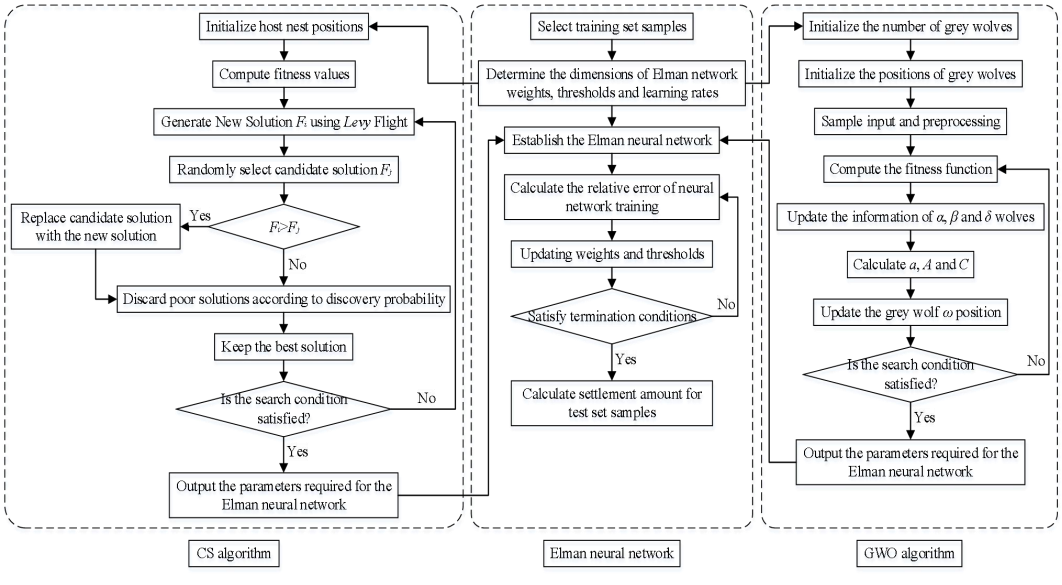

Figure 3: CS-Elman and GWO-Elman neural network flowchart.

https://doi.org/10.5194/egusphere-2024-1220
Preprint. Discussion started: 23 May 2024

3 Study area and data sources

3.1 Study area

The Wenchuan County in the Minjiang River Basin was greatly affected by the "5.12" earthquake, leading to a substantial increase in debris sources in the valley and an unusually intense activity of debris flows. Prior to the earthquake, there were no records of debris flow disasters in the valley, but in recent years, there have been several large-scale debris flows. The occurrence of debris flows in this area is closely related to rainfall and belongs to rainfall-induced landslide debris flows. This type of debris flow is initiated by heavy rainfall-induced slope movement, leading to the formation of debris flows.

This study selects the high mountain canyons on both sides of the Minjiang River and the Zagunao River as the study area. The river valley depression forms a "V"-shaped canyon with the Minjiang River as the boundary, representing a typical high mountain canyon. The location of the study area is shown in Figure 4. The terrain in this area is steep, with a maximum elevation difference of 4185 meters. Its unique terrain and geological structure result in frequent heavy rainfall, loose soil, and severe soil erosion. Consequently, geological disasters occur frequently in this area. Debris flow disasters have occurred in multiple valleys due to short-term heavy rainfall on July 10, 2013, August 20, 2019 and June 26, 2023, respectively (Ding and Huang, 2019; He et al., 2022a; Zhang et al., 2023).

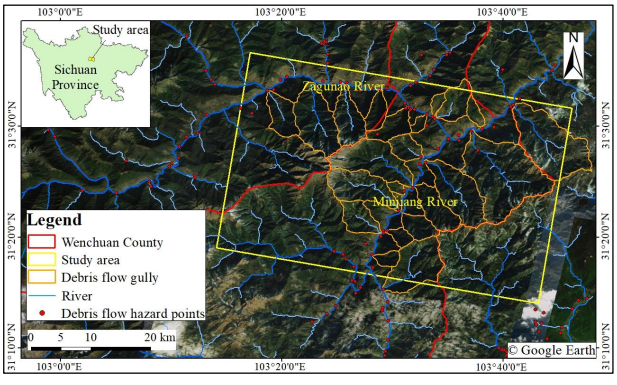

Figure 4: Location of study area. Source of optical background image: © Google Earth.

3.2 Data sources

The data mainly used in this study are 30 scenes of Sentinel-1A descending data from January 24, 2022 to December 21, 2023 downloaded from the alaska satellite facility (ASF). The data are acquired in interferometric wide (IW) mode, providing single look complex (SLC) images with a swath width of 250 km. The polarization mode is vertical-vertical (VV), with an incidence angle (angle between the transmission direction and the vertical direction) of 40.98°. The revisit period is 12 days, and the spatial resolution is 5 m × 20 m (range × azimuth), which is used to obtain the time-series deformation

https://doi.org/10.5194/egusphere-2024-1220
Preprint. Discussion started: 23 May 2024

information of the study area.

The auxiliary data include precise orbit determination (POD) data used to correct orbit information and improve the accuracy of image orbits, digital elevation model (DEM) data used to eliminate the influence of terrain phase in interferometric phase (Liao et al., 2013), google satellite images as auxiliary reference images, DEM, slope, aspect, curvature, soil type, TWI, SPI, surface roughness, terrain relief, FVC, rainfall, lithology and vegetation type used as evaluation factors for constructing predictive models. The data sources are shown in Table 2, the basic information of various data types is illustrated in Figure 5, and the classification of each factor is presented in Table 3.

Table 2: Data source parameter table.

Name of data	Temporality of data	Scale of data	Source of data
Sentinel-1A	Descending orbit from January 24, 2022 to December 21, 2023	5 m×20 m	Alaska satellite facility (ASF)
POD	Sentinel-1A image generation 21 days later	None	European space agency
DEM	In 2018	30 m	Japan aerospace exploration agency (JAXA)
Google satellite images	January 2022 to December 2023	1.07 m	Bigemap map downloader
Lithology and vegetation	In 2008	90 m	International soil reference and information centre
Slope, aspect, curvature, TWI, SPI, surface roughness and terrain relief	In 2018	30 m	Processed using ArcGIS to obtain DEM
Soil type	In 2009	90 m	National cryosphere desert data center
FVC	In 2019	30 m	Using ArcGIS to process Landsat 8-9 OLT/TIRS C2 L2 data downloaded from the Geospatial Data Cloud
Rainfall	January 2022 to December 2023	30 m	National earth system science data center

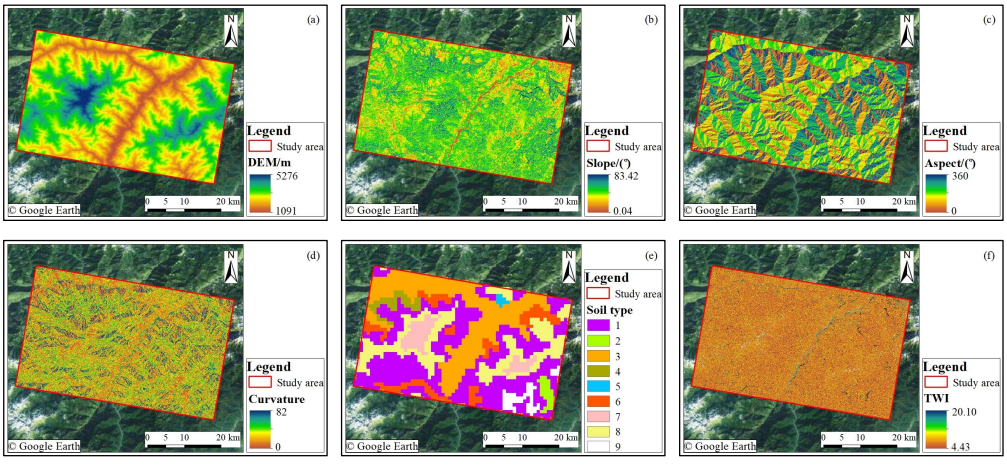

https://doi.org/10.5194/egusphere-2024-1220
Preprint. Discussion started: 23 May 2024

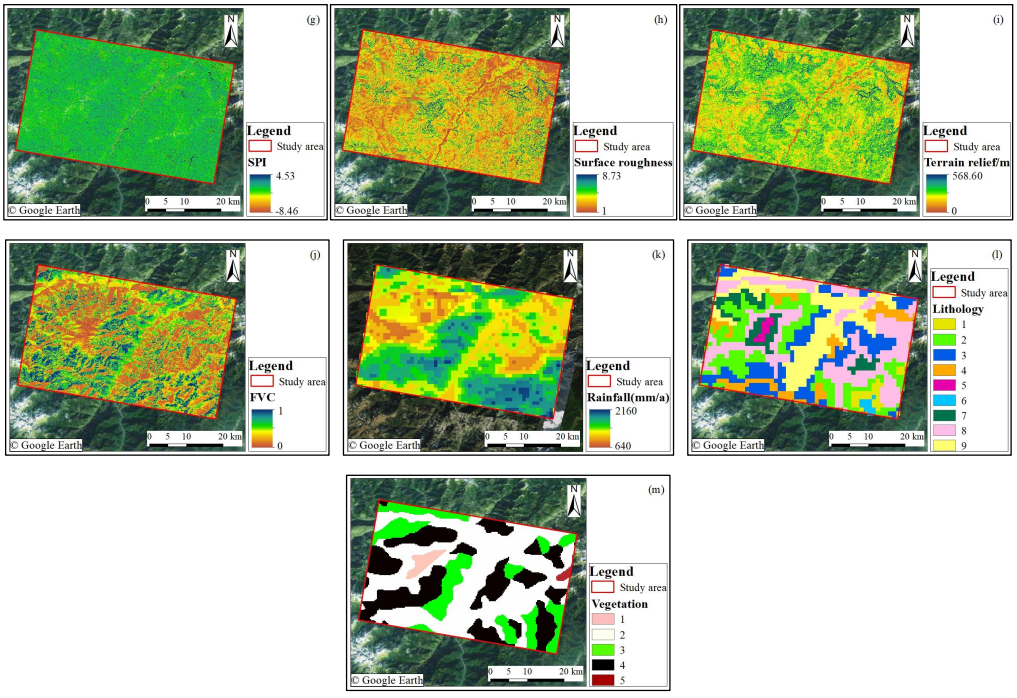

Figure 5: Layers of various factors. (a) DEM. (b) Slope. (c) Aspect. (d) Curvature. (e) Soil type. (f) TWI. (g) SPI. (h) Surface roughness. (i) Terrain relief. (j) FVC. (k) Rainfall. (l) Lithology. (m) Vegetation. Source of optical background image: © Google Earth.

Table 3: Classification status of various factors.

Evaluation factors	Number of classifications	Situation of classifications
DEM/m	5	(1)<2000 (2)2000~3000 (3)3000~4000 (4)4000~5000 (5)>5000
Slope/(°)	6	(1)Gentle slope to plain(<5°) (2)Slope(5°～15°) (3)Steep slope(15°～25°) (4)Sharp slope(25°～35°) (5)Steep and sharp slope(35°～55°) (6)Vertical slope(>55°)
Aspect/(°)	8	(1)N(0°~22.5°/337.5°~360°) (2)NE(22.5°~67.5°) (3)E(67.5°~112.5°) (4)SE(112.5°~157.5°) (5)S(157.5°~202.5°) (6)SW(202.5°~247.5°) (7)W(247.5°~292.5°) (8)NW(292.5°~337.5°)
Curvature	5	(1)0~10 (2)10~28 (3)28~46 (4)46~64 (5)64~82
Soil type	9	(1)LVh (2)PDd (3)CMc (4)GRh (5)RGd (6)RGe (7)LPi (8)LPm (9)CMd
TWI	5	(1)<8 (2)8~11 (3)11~14 (4)14~17 (5)>17
SPI	5	(1)<-6 (2)-6~-3 (3)-3~0 (4)0~3 (5)>3
Surface roughness	6	(1)1.0~2.5 (2)2.5~4.0 (3)4.0~5.5 (4)5.5~7.0 (5)7.0~8.5 (6)>8.5
Terrain relief/m	4	(1)Micro undulating terrain(<30) (2)Gentle undulating terrain(30~150) (3)Moderate undulating terrain(150~300) (4)Mountainous terrain(>300)
FVC	5	(1)0~0.2 (2)0.2~0.4 (3)0.4~0.6 (4)0.6~0.8 (5)0.8~1.0
Rainfall(mm/a)	5	(1)<800 (2)800~1200 (3)1200~1600 (4)1600~2000 (5)>2000
Lithology	9	(1)IA1 (2)MA2 (3)UE1 (4)SC2 (5)SO1 (6)SC4 (7)MB1 (8)MA3/MB1 (9)UR1
Vegetation	5	(1)Alpine vegetation (2)Grass clump (3)Deciduous forest (4)Coniferous forest (5)Meadow

https://doi.org/10.5194/egusphere-2024-1220
Preprint. Discussion started: 23 May 2024

4 Experimental results and analysis

4.1 Surface deformation monitoring experiment

The study utilizes the SBAS-InSAR and PS-InSAR techniques available in the Sarscape 5.6.2 module of ENVI 5.6.2 software to process Sentinel-1A images and extract deformation information in the study area. Taking into account factors such as temporal stability, land cover characteristics and data quality, the two time-series InSAR techniques select April 1, 2023 and December 26, 2022 as the master images, respectively. The annual average deformation rates in the radar line of sight (LOS) direction for the study area from January 24, 2022 to December 21, 2023 are shown in Figures 6 and 7, respectively. Positive values indicate uplift of the Earth's surface, meaning deformation towards the satellite's direction, while negative values indicate subsidence, meaning deformation away from the satellite's direction.

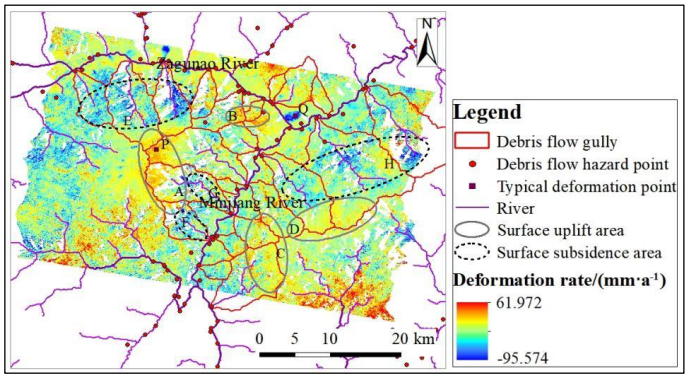

Figure 6: Annual average deformation rate map based on SBAS-InSAR.

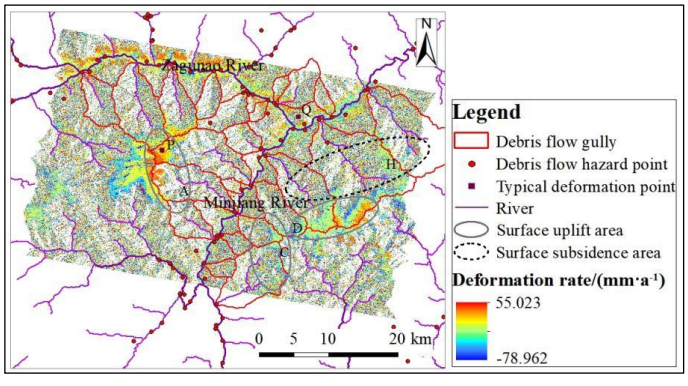

Figure 7: Annual average deformation rate map based on PS-InSAR.

https://doi.org/10.5194/egusphere-2024-1220
Preprint. Discussion started: 23 May 2024

In Figure 6, the SBAS-InSAR monitoring shows uplift in the upstream areas of various debris flow gullies, such as regions A, B, C and D, with the maximum uplift rate reaching 61.972 mm/a, located at the top of the main gully of Banzi Gully, indicated by point P in the figure. Additionally, different degrees of uplift are observed in the Zagunao River and Minjiang River channels. In the downstream areas of each debris flow gully, subsidence phenomena are observed, as seen in regions E, F, G and H, with the maximum subsidence rate reaching -95.574 mm/a, located at the confluence of the Minjiang and Zagunao rivers, indicated by point Q in the figure. In Figure 7, the PS-InSAR technology monitors the overall deformation rate in the study area, ranging from -78.962 mm/a to 55.023 mm/a. The monitoring effect is less satisfactory compared to SBAS-InSAR technology in areas with low coherence, resulting in fewer retrieved deformation information and greater influence from the geographical environment of the study area. However, PS-InSAR detects deformation patterns similar to those observed with SBAS-InSAR, such as uplift in regions A and D, as well as in the Zagunao River and Minjiang River channels, and subsidence in region H. According to field investigations, a debris flow disaster occurred on June 26, 2023 due to short-duration heavy rainfall, resulting in significant sediment deposition and uplift observed in the river channels.

For the typical deformation points P and Q, combined with rainfall data, a comparison of deformation trends is shown in Figure 8. Both time-series InSAR techniques monitor deformation points with roughly consistent trends exhibit nonlinear deformation patterns that correlate with rainfall and display seasonal variations. At point P, uplift increases with increasing rainfall, showing a distinct acceleration process. At point Q, the deformation trend is relatively flat during the rainy season, and as the rainy season recedes, the subsidence rate begins to accelerate. Moreover, the influence of rainfall on ground deformation is temporary, and after rainfall stops, the surface deformation will gradually return to the normal consolidation process.

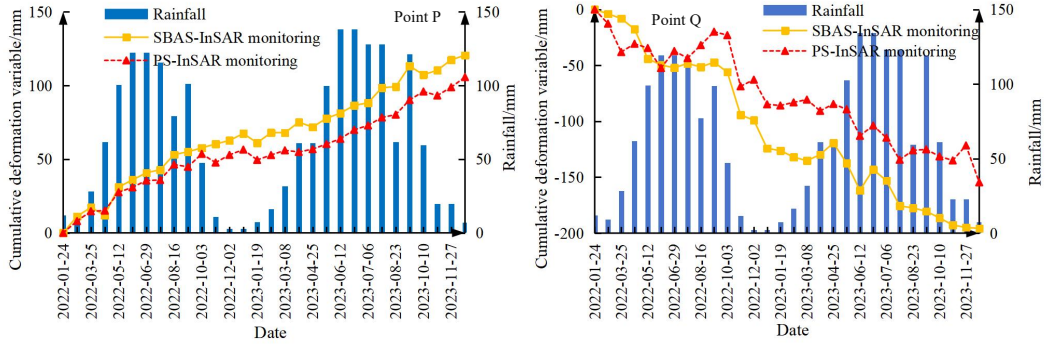

Figure 8: Comparison of deformation trends of typical deformation points monitored by two types of time-series InSAR techniques.

Although there are numerical and spatial differences in the final deformation rate results obtained from the two time-series

https://doi.org/10.5194/egusphere-2024-1220
Preprint. Discussion started: 23 May 2024

InSAR techniques, their deformation trends are generally consistent. To validate the reliability of the data, a cross-validation method was employed to verify the data before analysis. Several points with the same name were selected in the study area, and the annual average deformation values monitored by SBAS-InSAR and PS-InSAR techniques were taken as the x and y axes, respectively, for linear regression analysis. The results are shown in Figure 9. The correlation coefficient R^2=0.85 between the LOS deformation rates of the same-named points monitored by the two data sets indicates a high correlation between the data monitored by the two InSAR techniques, demonstrating the feasibility of joint analysis using both techniques.

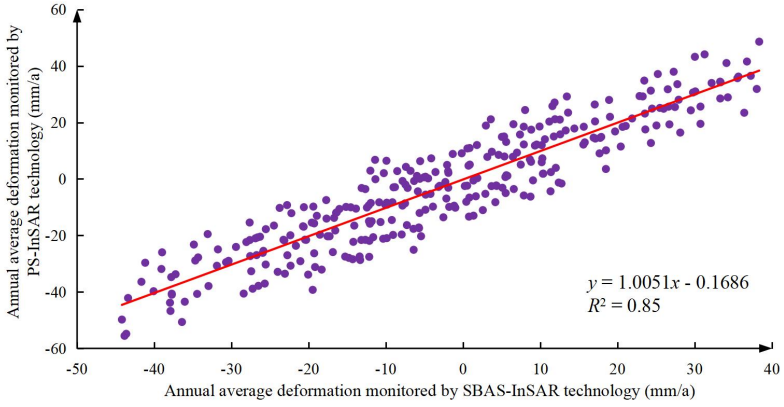

Figure 9: Cross validation results of LOS deformation rate using time series InSAR technology.

In addition, the study area has high vegetation coverage, causing scattering, occlusion and interference of radar signals along the propagation path, leading to severe decorrelation and affecting the accuracy of deformation monitoring. Therefore, the FVC is introduced to analyze the vegetation coverage in the study area. For areas with an FVC greater than 0.6, the deformation points are not selected to eliminate the influence of high vegetation coverage on deformation monitoring in the study area.

4.2 Surface deformation prediction experiment

4.2.1 The impact of CS/GWO algorithm on the performance of Elman network

In this study, ArcGIS software is used to extract the layer data of 13 evaluation factors in the research area. In order to assess whether these 13 evaluation factors are suitable as predictors for surface deformation in high mountain gorges, grey relational analysis is conducted using SPSSAU software to analyze the grey relational values between each of the 13 factors and the annual average deformation values monitored by the InSAR technology. The grey relational values are presented in Table 4.

https://doi.org/10.5194/egusphere-2024-1220
Preprint. Discussion started: 23 May 2024

Table 4: The grey relational coefficient between each factor and the deformation value.

Evaluation factor	Grey relational values	Evaluation factor	Grey relational values
DEM	0.809	Surface roughness	0.804
Slope	0.803	Terrain relief	0.789
Aspect	0.803	FVC	0.806
Curvature	0.804	Rainfall	0.807
Soil type	0.779	Lithology	0.794
TWI	0.786	Vegetation	0.825
SPI	0.799		

The grey relational values indicate a high degree of correlation between the selected 13 evaluation factors and the deformation values. However, the final factors have not yet been selected. In order to obtain the optimal evaluation factors to prevent problems such as overfitting and instability caused by strong correlations between factors, a correlation matrix analysis is conducted on each factor (Dziuban and Shirkey, 1974). The results are shown in Table 5.

Table 5: Correlation coefficients among various factors.

Factor	DEM	Slope	Aspect	Curvature	Soil type	TWI	SPI	Surface roughness	Terrain relief	FVC	Rainfall	Lithology	Vegetation
DEM	1												
Slope	-0.08	1											
Aspect	-0.01	0.07	1										
Curvature	0.14	-0.20	-0.01	1									
Soil type	0.59	-0.12	0.06	0.13	1								
TWI	-0.01	-0.47	-0.06	0.11	0.05	1							
SPI	0.05	0.30	-0.03	0.01	0.01	-0.03	1						
Surface roughness	-0.12	0.82	0.08	-0.16	-0.10	-0.42	0.25	1					
Terrain relief	-0.11	0.85	0.07	-0.18	-0.11	-0.43	0.29	0.97	1				
FVC	-0.22	0.01	-0.55	-0.22	-0.22	-0.04	-0.16	0.04	0.04	1			
Rainfall	-0.30	0.07	-0.05	-0.15	-0.38	-0.01	-0.12	0.06	0.06	0.31	1		
Lithology	-0.12	-0.15	0.07	0.02	0.22	0.04	0.09	-0.11	-0.09	-0.13	-0.22	1	
Vegetation	-0.20	0.04	0.05	0.02	-0.13	-0.05	-0.09	0.04	0.04	0.16	0.24	-0.15	1

From Table 5, it can be observed that the correlation coefficients $|R|$ between DEM and soil type, slope and surface roughness, terrain relief, and aspect and FVC are greater than 0.5, indicating strong correlations. Therefore, highly correlated influencing factors are removed. Consequently, DEM, slope, curvature, TWI, SPI, FVC, rainfall, lithology and vegetation type are selected as evaluation factors for the CS/GWO-Elman model.

The 9 selected evaluation factors are used to construct the CS/GWO-Elman model along with the annual average

https://doi.org/10.5194/egusphere-2024-1220
Preprint. Discussion started: 23 May 2024

deformation rate values extracted by the InSAR technique in the study area. A total of 1000 points are randomly selected as samples for the CS/GWO-Elman neural network, and predictions are made for 30 of these sample points. To ensure comparability between the Elman networks optimized by CS and GWO, a CS/GWO-Elman network model is constructed using Matlab software, and various parameters are standardized. The functions of each network layer are shown in Table 6, while the network training parameters are presented in Table 7.

Table 6: CS/GWO-Elman neural network functions in each layer.

The functions of each layer in the network	Function settings
Training function	trainlm
The activation function of the hidden layer	tanh
The activation function of the output layer	purelin

Table 7: CS/GWO-Elman network training parameters.

Parameter names	Setting values	Parameter names	Setting values
Training epochs	1000	Maximum evolutionary generations	50
Learning rate	0.01	initial population size for CS	10
Minimum training target error	10^{-5}	probability of discovering a cuckoo egg by CS	0.25
Display frequency	25	number of searching wolves in GWO	20
Momentum factor	0.01	range of searching for wolves in GWO	30

The randomly selected samples are input into the Elman, CS-Elman and GWO-Elman models, and their predicted results are compared with the annual average deformation rate results monitored by InSAR, as shown in Figure 10. It can be clearly seen that the predicted curves of the three network models are generally consistent with the InSAR monitoring curve. By calculating the absolute error between the predicted values of each model and the monitored values of InSAR, as shown in Figure 11, the absolute error ranges of Elman, CS-Elman and GWO-Elman models with InSAR monitoring of the annual average deformation rate are 0.205 to 7.733 mm/a, 0.016 to 4.576 mm/a and 0.193 to 6.292 mm/a, respectively. The absolute error range of the CS-improved Elman network is smaller. It is also evident that the absolute error curve of the CS-Elman prediction is closer to the horizontal axis and has a smaller amplitude, indicating better prediction results.

https://doi.org/10.5194/egusphere-2024-1220
Preprint. Discussion started: 23 May 2024

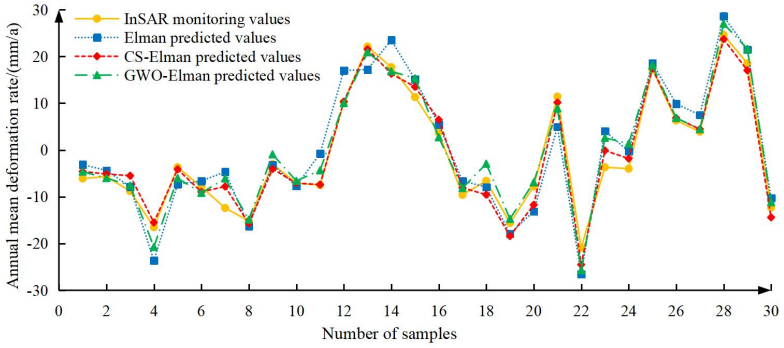

Figure 10: Comparison of the predicted values from the three models with the monitored values from InSAR.

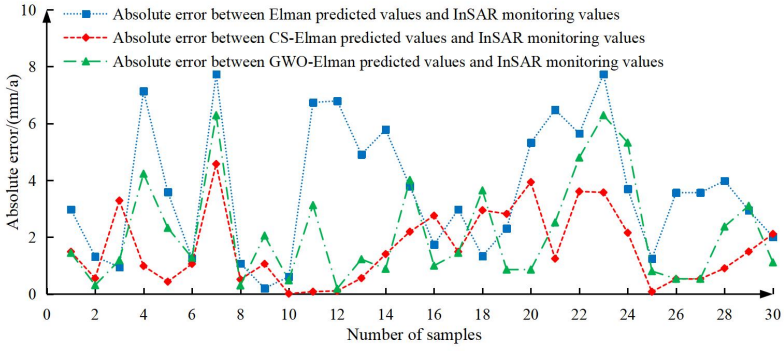

385

Figure 11: Comparison of absolute errors among three models.

To validate the predictive performance under different optimization algorithms, the mean squared error (Hodson et al., 2021) and the optimal number of iterations for each group are calculated, as shown in Figure 12. The optimal convergence 390 iterations for Elman, CS-Elman and GWO-Elman networks are 19, 3 and 5 times, respectively, with mean squared errors of 0.033, 0.020 and 0.030 mm/a, respectively. The Elman network improved by CS converges faster with a smaller mean squared error, validating that the CS algorithm can overcome the slow convergence and low learning rate of Elman neural networks.

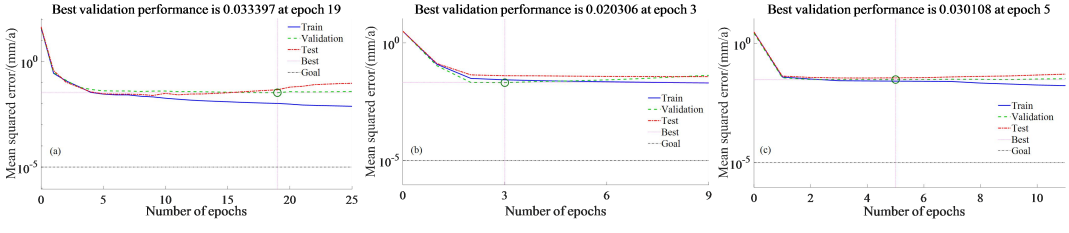

395

Figure 12: Mean square error and optimal iteration numbers of the three models. (a) is Elman model, (b) is CS-Elman model, (c) is GWO-Elman model.

https://doi.org/10.5194/egusphere-2024-1220
Preprint. Discussion started: 23 May 2024

To validate the reliability of prediction accuracy under different optimization algorithms, the mean absolute error (MAE) (Chai and Draxler, 2014) and mean absolute percentage error (MAPE) (De et al., 2016) are used as evaluation metrics. The smaller the values of these evaluation metrics, the smaller the prediction error of the model, indicating a better fit to the data. MAE represents the average of the absolute errors between the InSAR monitoring values and the corresponding model predicted values, calculated using the formula as equation (11). Here, n denotes the number of samples, y_i represents the InSAR monitoring values, and $\hat{y}_i$ represents the predicted values of the corresponding network.

$$MAE = \frac{1}{n}\sum_{i=1}^{n}|y_i - \hat{y}_i| \tag{11}$$

MAPE represents the mean absolute percentage difference between the InSAR monitoring values and the corresponding model predicted values, calculated using the formula as equation (12):

$$MAPE = \frac{1}{n}\sum_{i=1}^{n}\left|\frac{y_i - \hat{y}_i}{y_i}\right| \times 100\% \tag{12}$$

The comparison of evaluation indicators for each group of data is shown in Table 8. Through comparison, it is found that both CS and GWO algorithms can effectively improve the prediction performance and accuracy of the Elman network. Moreover, the CS-Elman model has smaller MAE and MAPE, indicating higher prediction accuracy. Thus, it is demonstrated that utilizing the CS algorithm to improve the Elman neural network leads to better prediction performance and accuracy for surface deformation in high mountain gorges.

Table 8: Comparison of evaluation metrics for the three models.

Evaluation indicators	Elman	CS-Elman	GWO-Elman
MAE/(mm/a)	3.650	1.620	2.155
MAPE/%	44.663	21.500	29.689

4.2.2 Model comparison analysis experiment

To further verify the superiority of the CS-Elman model in predicting surface deformation in high mountain gorges, we select the SVM, LSTM and GA-BP (Yang et al., 2022) models and compared them with the CS-Elman model in a comparative experiment. In the comparative experiment, we use the same 9 factors including DEM and the time-series of annual average deformation rates extracted by InSAR technology as data. We randomly select 507 sample data points, with 500 used for training and the remaining 7 for prediction. The prediction results of each model after training are shown in Figure 13, the absolute errors between the predicted values and the InSAR monitoring values are shown in Figure 14, and the performance comparison is shown in Table 9.

https://doi.org/10.5194/egusphere-2024-1220
Preprint. Discussion started: 23 May 2024

425

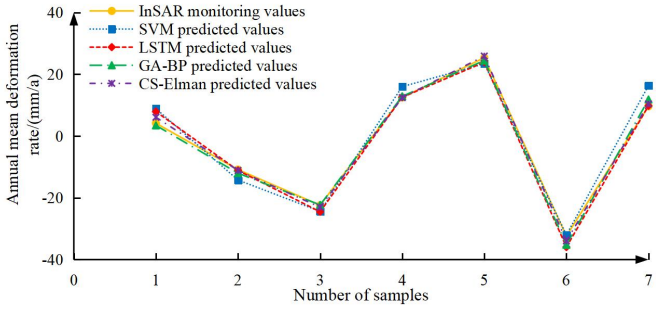

Figure 13: Comparison between the predicted values of each model and the monitored values from InSAR.

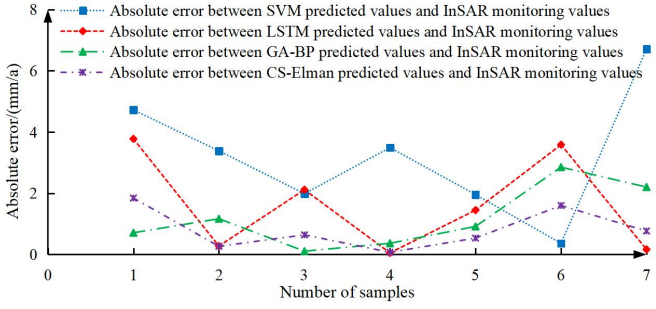

430 **Figure 14: Absolute error between predicted values of each model and the monitored values from InSAR.**

Table 9: Comparison of performance metrics for each model.

Model	Evaluation indicators			
	MAE/(mm/a)	MAPE/%	Convergence optimal iteration times	Mean squared error/(mm/a)
SVM	3.231	37.241%	23	0.031
LSTM	1.631	17.458%	10	0.033
GA-BP	1.189	9.521%	7	0.029
CS-Elman	0.818	9.353%	3	0.024

In Figure 13, the predicted curves of each model align closely with the InSAR monitoring curve. As shown in Figure 14 and
435 Table 9, the prediction errors of each model are within 7 mm/a. Compared to other models, the CS-Elman model exhibits the smallest range of prediction absolute error, ranging from 0.071 to 1.843 mm/a. Additionally, the CS-Elman model has a lower MAE of 0.818 mm/a and MAPE of 9.353%, both smaller than those of other models, indicating higher prediction accuracy. Moreover, the CS-Elman model demonstrates faster convergence speed and smaller mean squared error, validating its superiority and effectiveness in predicting surface deformation in high mountain gorge areas.

https://doi.org/10.5194/egusphere-2024-1220
Preprint. Discussion started: 23 May 2024

4.2.3. Deformation prediction analysis

Through the above experimental analysis, it has been verified that the Elman neural network optimized by the CS algorithm has superior predictive performance. Therefore, a time-series deformation prediction is conducted on the typical deformation points P and Q. Since the same deformation point is independent of DEM, slope, curvature, FVC, lithology and vegetation type, time-series data such as TWI, SPI and rainfall are selected. A CS-Elman model is constructed using the time-series deformation variables monitored by InSAR technology. A total of 26 periods of data from January 24, 2022 to September 16, 2023 are selected as training samples, and the CS-Elman model is used to predict the deformation values for the subsequent 4 periods. The predicted deformation values compared with the InSAR monitoring values are shown in Table 10.

Table 10: Comparison between predicted values and monitored values.

	Periods	20231010	20231103	20231127	20231221
Point P	InSAR monitoring values/mm	107.391	110.315	117.408	120.557
	CS-Elman predicted values/mm	111.354	112.032	118.183	117.184
	Absolute error/mm	3.963	1.717	0.775	3.373
Point Q	InSAR monitoring values/mm	-186.347	-192.725	-194.912	-195.748
	CS-Elman predicted values/mm	-187.706	-190.148	-194.229	-200.528
	Absolute error/mm	1.359	2.577	0.683	4.780

According to Table 10, the average absolute errors between the predicted values and monitored values for points P and Q are 2.457 mm and 2.350 mm, respectively. According to the *Technical Specification for Ground Subsidence Measurement* (DZ/T0154-2020) released by the ministry of natural resources of China, the accuracy of InSAR deformation is $\pm$10 mm, and the prediction accuracy meets the requirements of the measurement specifications. Thus, it is confirmed that the combination of time-series InSAR technology and the CS-Elman algorithm can effectively monitor and predict the deformation values of points in high mountain gorges.

5 Conclusion

This study proposes an improved prediction method for surface deformation in high mountain gorges using the multi-factor and multi-temporal approach based on surface deformation values monitored by time-series InSAR technology and factors such as DEM. It effectively addresses the issues of excessive dependence on deformation data and singularity in existing prediction models. Experimental comparisons reveal the following findings:

(1) The correlation coefficient R^2 between the LOS deformation velocities of the same points monitored by SBAS-InSAR and PS-InSAR technologies is 0.85, indicating a high level of correlation and demonstrating the feasibility of jointly analyzing surface deformation using these two techniques.

https://doi.org/10.5194/egusphere-2024-1220
Preprint. Discussion started: 23 May 2024

(2) Predictions for 30 sample sets indicate that both CS-Elman and GWO-Elman models exhibit improved performance compared to Elman alone, demonstrating that both CS and GWO algorithms effectively enhance the predictive performance and accuracy of the Elman model. Specifically, the CS-Elman model shows smaller absolute errors, fewer optimal convergence iterations, and lower mean square errors compared to the GWO-Elman network. The MAE for CS-Elman and GWO-Elman models are 1.620 mm/a and 2.155 mm/a, respectively, while the MAPE are 21.500% and 29.689%, respectively. The smaller MAE and MAPE of the CS-Elman model indicate higher prediction accuracy. This validates that utilizing the CS algorithm to improve the Elman model results in better predictive performance and effectiveness for surface deformation in high mountainous areas.

(3) By comparing the optimal CS-Elman model with SVM, LSTM and GA-BP, we verify the advantages and effectiveness of the model in predicting surface deformation in high mountainous areas. Utilizing time-series data such as TWI, SPI and rainfall, combined with the time-series deformation variables monitored by InSAR technology, the deformation trend predictions for typical deformation points P and Q show that the average absolute errors for the 4-period predictions compared to the monitored values are 2.457 mm and 2.350 mm, respectively. This validates that using time-series InSAR technology and the CS-Elman model can effectively monitor and predict the deformation values of a specific point.

The methodology presented in this paper, while comprehensive in considering influencing factors and time-series data, also has some limitations. For instance, the lack of concurrent leveling data prevents accurate validation of the results obtained. Moreover, the study only provides a preliminary investigation into surface deformation in the Minjiang River Basin, with limited research on typical deformation areas. Subsequent studies will further explore whether the CS-Elman model is applicable to deformation prediction in other regions. Additionally, the accuracy of time-series InSAR monitoring is significantly influenced by the resolution of the DEM. Therefore, future efforts will focus on utilizing higher-resolution DEM to enhance the accuracy of subsidence monitoring.

Code and Data availability

The code and data that support the findings of this study are available from the corresponding author upon reasonable request.

Sentinel-1A data is acquired from the Alaska Satellite Facility (ASF) and the link is https://search.asf.alaska.edu/.

POD data is acquired from the European Space Agency (ESA) and the link is https://step.esa.int/.

DEM data is acquired from the Japan Aerospace Exploration Agency (JAXA) and the link is https://www.eorc.jaxa.jp/ALOS/en/aw3d30/data/index.htm.

Rainfall data is acquired from the National Earth System Science Data Center (NESSDC) and the link is http://www.geodata.cn/data/.

https://doi.org/10.5194/egusphere-2024-1220
Preprint. Discussion started: 23 May 2024

Lithology and vegetation data are acquired from the International Soil Reference and Information Centre (ISRIC) and the link is https://www.isric.org.

Soil data is acquired from the National Cryosphere Desert Data Center and the link is https://www.ncdc.ac.cn/.

Landsat8-9 OLT/TIRS C2 L2 data is acquired from the Geospatial Data Cloud and the link is https://www.gscloud.cn/.

Author contributions

Kuayue Chen: conceptualization, methodology, visualization, writing and editing. Wenfei Xi: methodology and review. Baoyun Wang: conceptualization, methodology and review.

Competing interests

The contact author has declared that none of the authors has any competing interests.

Financial support

This work was supported by National Natural Science Foundation of China: [Grant Number 61966040].

References

Akritas, A. G., and Malaschonok, G. I.: Applications of singular-value decomposition (SVD), Math. Comput. Simulat., 67, 15-31, https://doi.org/10.1016/j.matcom.2004.05.005, 2004.

An, B. S., Wang, W. C., Yang, W., Wu, G. J., Guo, Y. H., Zhu, H. F., Gao, Y., Bai, L., Zhang, F., Zeng, C., Wang, L., Zhou, J., Li, X., Li, J., Zhao, Z. J., Chen, Y. Y., Liu, J. S., Li, J. L., Wang, Z. Y., Chen, W. F., and Yao, T. D.: Process, mechanisms, and early warning of glacier collapse-induced river blocking disasters in the Yarlung Tsangpo Grand Canyon, southeastern Tibetan Plateau, Sci. Total Environ., 816, 151652, https://doi.org/10.1016/j.scitotenv.2021.151652, 2022.

Berardino, P., Fornaro, G., Lanari, R., and Sansosti, E.: A new algorithm for surface deformation monitoring based on small baseline differential SAR interferograms, IEEE T. Geosci. Remote, 40, 2375-2383, https://doi.org/10.1109/TGRS.2002.803792, 2002.

Chai, T., and Draxler, R. R.: Root mean square error (RMSE) or mean absolute error (MAE)?–Arguments against avoiding RMSE in the literature, Geosci. Model Dev., 7, 1247-1250, https://doi.org/10.5194/gmd-7-1247-2014, 2014.

De Myttenaere, A., Golden, B., Le Grand, B., and Rossi, F.: Mean absolute percentage error for regression models, Neurocomputing, 192, 38-48, https://doi.org/10.1016/j.neucom.2015.12.114, 2016.

Derbyshire, E.: Geological hazards in loess terrain, with particular reference to the loess regions of China, Earth-Sci. Rev., 54, 231-260, https://doi.org/10.1016/S0012-8252(01)00050-2, 2001.

https://doi.org/10.5194/egusphere-2024-1220
Preprint. Discussion started: 23 May 2024

Ding, M. T., and Huang, T.: Vulnerability assessment of population in mountain settlements exposed to debris flow: a case study on Qipan gully, Wenchuan County, China, Nat. Hazards, 99, 553-569, https://doi.org/10.1007/s11069-019-03759-1, 2019.

Ding, S. F., Zhang, Y. N., Chen, J. R., and Jia, W. K.: Research on using genetic algorithms to optimize Elman neural networks, Neural Comput. Appl., 23, 293-297, https://doi.org/10.1007/s00521-012-0896-3, 2013.

Dziuban, C. D., and Shirkey, E. C.: When is a correlation matrix appropriate for factor analysis? Some decision rules, Psychol. Bull., 81, 358, https://doi.org/10.1037/h0036316, 1974.

Elman, J. L.: Finding structure in time, Cognitive Sci., 14, 179-211, https://doi.org/10.1207/s15516709cog1402_1, 1990.

Ferretti, A., Prati, C., and Rocca, F.: Permanent scatterers in SAR interferometry, IEEE T. Geosci. Remote, 39, 8-20, https://doi.org/10.1109/36.898661, 2001.

Guo, X. J., Cui, P., Li, Y., Zou, Q., and Kong, Y. D.: The formation and development of debris flows in large watersheds after the 2008 Wenchuan Earthquake, Landslides, 13, 25-37, https://doi.org/10.1007/s10346-014-0541-6, 2016.

Gupta, S., and Deep, K.: A novel random walk grey wolf optimizer, Swarm Evol. Comput., 44, 101-112, https://doi.org/10.1016/j.swevo.2018.01.001, 2019.

He, J., Zhang, L. M., Fan, R. L., Zhou, S. Y., Luo, H. Y., and Peng, D. L.: Evaluating effectiveness of mitigation measures for large debris flows in Wenchuan, China, Landslides, 19, 913-928, https://doi.org/10.1007/s10346-021-01809-z, 2022a.

He, M. C., Sui, Q. R., Li, M. N., Wang, Z. J., and Tao, Z. G.: Compensation excavation method control for large deformation disaster of mountain soft rock tunnel, Int. J. Min. Sci. Techno., 32, 951-963, https://doi.org/10.1016/j.ijmst.2022.08.004, 2022b.

Hodson, T. O., Over, T. M., and Foks, S. S.: Mean squared error, deconstructed, J. Adv. Model. Earth Sy., 13, e2021MS002681, https://doi.org/10.1029/2021MS002681, 2021.

Huang Lin, C., Liu, D. W., and Liu, G.: Landslide detection in La Paz City (Bolivia) based on time series analysis of InSAR data, Int. J. Remote Sens., 40, 6775-6795, https://doi.org/10.1080/01431161.2019.1594434, 2019.

Jia, W. K., Zhao, D. A., Zheng, Y. J., and Hou, S. J.: A novel optimized GA–Elman neural network algorithm, Neural Comput. Appl., 31, 449-459, https://doi.org/10.1007/s00521-017-3076-7, 2019.

Jiang, N., Li, H. B., Li, C. J., Xiao, H. X., and Zhou, J. W.: A fusion method using terrestrial laser scanning and unmanned aerial vehicle photogrammetry for landslide deformation monitoring under complex terrain conditions, IEEE T. Geosci. Remote, 60, 1-14, https://doi.org/10.1109/TGRS.2022.3181258, 2022.

Kim, D., Langley, R. B., Bond, J., and Chrzanowski, A.: Local deformation monitoring using GPS in an open pit mine: initial study, GPS Solut., 7, 176-185, https://doi.org/10.1007/s10291-003-0075-1, 2003.

Lanari, R., Mora, O., Manunta, M., Mallorquí, J. J., Berardino, P., and Sansosti, E.: A small-baseline approach for investigating deformations on full-resolution differential SAR interferograms, IEEE T. Geosci. Remote, 42, 1377-1386,

https://doi.org/10.5194/egusphere-2024-1220
Preprint. Discussion started: 23 May 2024

https://doi.org/10.1109/TGRS.2004.828196, 2004.

Liao, M. S., Jiang, H. J., Wang, Y., Wang, T., and Zhang, L.: Improved topographic mapping through high-resolution SAR interferometry with atmospheric effect removal, ISPRS J. Photogramm., 80, 72-79, https://doi.org/10.1016/j.isprsjprs.2013.03.008, 2013.

Liu, C. X., & Wang, B. Y.: Gully-type debris flow susceptibility assessment based on a multi-channel multi-scale residual network fusing multi-source data: a case study of Nujiang Prefecture, All Earth, 36, 1-18, https://doi.org/10.1080/27669645.2023.2292311, 2024.

Mareli, M., and Twala, B.: An adaptive Cuckoo search algorithm for optimisation, Applied computing and informatics, 14, 107-115, https://doi.org/10.1016/j.aci.2017.09.001, 2018.

Mirjalili, S., Mirjalili, S. M., and Lewis, A.: Grey wolf optimizer, Adv. Eng. Softw., 69, 46-61, https://doi.org/10.1016/j.advengsoft.2013.12.007, 2014.

Nikolaeva, E., Walter, T. R., Shirzaei, M., and Zschau, J.: Landslide observation and volume estimation in central Georgia based on L-band InSAR, Nat. Hazards Earth Syst. Sci., 14, 675-688, https://doi.org/10.5194/nhess-14-675-2014, 2014.

Osmanoğlu, B., Sunar, F., Wdowinski, S., and Cabral-Cano, E.: Time series analysis of InSAR data: Methods and trends, ISPRS J. Photogramm., 115, 90-102, https://doi.org/10.1016/j.isprsjprs.2015.10.003, 2016.

Radman, A., Akhoondzadeh, M., and Hosseiny, B.: Integrating InSAR and deep-learning for modeling and predicting subsidence over the adjacent area of Lake Urmia, Iran, GISci. Remote Sens., 58, 1413-1433, https://doi.org/10.1080/15481603.2021.1991689, 2021.

Suresh, D., and Yarrakula, K.: InSAR based deformation mapping of earthquake using Sentinel 1A imagery, Geocarto Int., 35, 559-568, https://doi.org/10.1080/10106049.2018.1544289, 2020.

Tao, Z. G., Zhu, C., He, M. C., and Karakus, M.: A physical modeling-based study on the control mechanisms of Negative Poisson's ratio anchor cable on the stratified toppling deformation of anti-inclined slopes, Int. J. Rock Mech. Min., 138, 104632, https://doi.org/10.1016/j.ijrmms.2021.104632, 2021.

Teng, C. Q., Wang, L., and Jiang, C.: Urban surface deformation monitoring and prediction by integrating SBAS-InSAR and Elman neural network, Surv. Rev., 56, 18-31, https://doi.org/10.1080/00396265.2022.2157119, 2024.

Ulusay, R., Türeli, K., and Ider, M. H.: Prediction of engineering properties of a selected litharenite sandstone from its petrographic characteristics using correlation and multivariate statistical techniques, Eng. Geol., 38, 135-157, https://doi.org/10.1016/0013-7952(94)90029-9, 1994.

Vanicek, P., Castle, R. O., and Balazs, E. I.: Geodetic leveling and its applications, Rev. Geophys., 18, 505-524, https://doi.org/10.1029/RG018i002p00505, 1980.

Wang, Y. Y., Guo, Y. H., Hu, S. Q., Li, Y., Wang, J. Z., Liu, X. S., and Wang, L.: Ground deformation analysis using InSAR and backpropagation prediction with influencing factors in Erhai Region, China, Sustainability-basel, 11, 2853,

https://doi.org/10.3390/su11102853, 2019.

Wang, Z. D., Wen, X. H., Tang, W., Liu, H., and Wang, D. F.: Early detection of geological hazards in Longmenshan-Dadu river area using various InSAR techniques, Geomatics and Information Science of Wuhan University, 45, 451-459, https://doi.org/10.13203/j.whugis20190064, 2020.

Xu, F. S., and Wang, B. Y.: Debris flow susceptibility mapping in mountainous area based on multi-source data fusion and CNN model–taking Nujiang Prefecture, China as an example, Int. J. Digit. Earth, 15, 1966-1988, https://doi.org/10.1080/17538947.2022.2142304, 2022.

Yang, X. S., and Deb, S.: Cuckoo search via Lévy flights, In 2009 World congress on nature & biologically inspired computing (NaBIC), 210-214, Ieee, https://doi.org/10.1109/NABIC.2009.5393690, 2009.

Yang, Z. F., Li, Z. W., Zhu, J. J., Wang, Y. D., and Wu, L. X.: Use of SAR/InSAR in mining deformation monitoring, parameter inversion, and forward predictions: A review, IEEE Geosc. Rem. Sen. M., 8, 71-90, https://doi.org/10.1109/MGRS.2019.2954824, 2020.

Yang, Z. L., Lu, H., Zhang, Z. J., Liu, C., Nie, R. H., Zhang, W. C., Fan, G., Chen, C., Ma, L., Dai, X. A., Zhang, M., and Zhang, D. H.: Visualization analysis of rainfall-induced landslides hazards based on remote sensing and geographic information system-an overview, Int. J. Digit. Earth, 16, 2374-2402, https://doi.org/10.1080/17538947.2023.2229797, 2023.

Yang, Z. R., Xi, W. F., Yang, Z. Q., Shi, Z. T., and Qian, T. H.: Monitoring and prediction of glacier deformation in the meili snow mountain based on InSAR technology and GA-BP neural network algorithm, Sensors-basel, 22, 8350, https://doi.org/10.3390/s22218350, 2022.

Ye, Y. C., Yan, C. D., Luo, X. X., Zhang, R. F., and Yuan, G. J.: Analysis of ground subsidence along Zhengzhou metro based on time series InSAR, National Remote Sensing Bulletin, 26, 1342-1353, https://doi.org/10.11834/jrs.20211246, 2022.

Zhang, G., Wang, S. Y., Chen, Z. W., Zheng, Y. Z., Zhao, R. S., Wang, T. Y., Zhu, Y., Yuan, X. Z., Wu, W., and Chen, W. T.: Development of China's spaceborne SAR satellite, processing strategy, and application: take Gaofen-3 series as an example, Geo-spat. Inf. Sci., 27, 221-236, https://doi.org/10.1080/10095020.2022.2124129, 2024.

Zhang, Z. J., Lin, H., Wang, M. M., Liu, X. G., Chen, Q. H., Wang, C., and Zhang, H.: A review of satellite synthetic aperture radar interferometry applications in permafrost regions: Current status, challenges, and trends, IEEE Geosc. Rem. Sen. M., 10, 93-114, https://doi.org/10.1109/MGRS.2022.3170350, 2022.

Zhang, X. Z., Tie, Y. B., and Ning Z. J.: Characteristics and activity analysis of the catastrophic "6· 26" debris flow in the Banzi Catchment, Wenchuan County of Sichuan Province, Hydrogeology & Engineering Geology, 50, 134-145, https://doi.cnki.net/10.16030/j.cnki.issn.1000-3665.202307003, 2023.